




Improvements of diagnostic accuracy and visualization of vertebral metastasis using multi-level virtual non-calcium reconstructions from dual-layer spectral detector computed tomography

N. Abdullayev¹ · N. Große Hokamp^{1,2,3,4}  · S. Lennartz¹ · J. A. Holz¹ · Z. Romman⁵ · G. Pahn⁶ · V. Neuhaus¹ · D. Maintz¹ · B. Krug¹ · J. Borggrefe¹

Received: 3 January 2019 / Revised: 5 April 2019 / Accepted: 9 April 2019 / Published online: 30 April 2019
© European Society of Radiology 2019

Abstract

Objective To evaluate feasibility and diagnostic performance of multi-level calcium suppression in spectral detector computed tomography (SDCT) for assessment of bone metastasis.

Materials and methods Retrospective IRB-approved study on 21 patients who underwent SDCT (120 kV, reference mAs 116) and MRI. Thoracic and lumbar vertebrae ($n = 357$) were included and categorized as normal ($n = 133$) or metastatic ($n = 203$) based on MRI (STIR, T1w, \pm contrast). The multi-level virtual non-calcium (VNCa) algorithm computes dynamic soft tissue/calcium pairs allowing for computation of different suppression index levels to address inter-individual variance of prevalent calcium composition weights. We computed images with low, medium, and high calcium suppression indices and compared them with conventional images (VNCa_low/med/high and conventional images (CI)). For quantitative image analysis, regions of interest were placed in normal and metastatic bone. Two readers reviewed the datasets independently in multiple sessions. They determined the presence of vertebral metastases on a per vertebra basis using a binary scale. Statistic assessment was performed using ANOVA with Tukey HSD, Student's T test, and ROC analysis.

Results Attenuation of both normal and metastatic bone was lower in VNCa images than that in conventional images (e.g., CI/VNCa_low, -46.3 to 238.8 HU/ 343.3 – 60.2 HU; $p \leq 0.05$). VNCa_low+med improved separation of normal and metastatic bone in ROC analysis (AUC, CI/VNCa_low/VNCa_med = $0.74/0.95/0.98$; $p \leq 0.05$). In subjective analysis, both sensitivity and specificity were clearly improved in VNCa_low as compared with CI ($0.85/0.84$ versus $0.78/0.82$). Readers showed a good inter-rater reliability ($\kappa = 0.65$).

Conclusions Multi-level VNCa reconstructed from SDCT improve quantitative separation of normal and metastatic bone and subjective determination of bone metastases when using low to intermediate calcium suppression indices.

Key Points

- Spectral detector CT allows for multi-level calcium suppression in CT images and low and medium calcium suppression indices improved separation of normal and metastatic bone.
- Thus, multi-level calcium suppression allows to optimize image contrast in regard to dedicated pathologies.
- Low-level virtual non-calcium images (index 25–50) improved diagnostic performance regarding detection of metastasis.

N. Abdullayev and N. Große Hokamp contributed equally to this work.

Electronic supplementary material The online version of this article (<https://doi.org/10.1007/s00330-019-06233-5>) contains supplementary material, which is available to authorized users.

✉ N. Große Hokamp
nils.grosse-hokamp@uk-koeln.de

¹ Institute for Diagnostic and Interventional Radiology, University Hospital Cologne, Cologne, Germany

² Department of Radiology, Case Western Reserve University, Cleveland, OH, USA

³ Department of Radiology, University Hospitals Medical Center, Cleveland, OH, USA

⁴ Department of Diagnostic and Interventional Radiology, University Hospital Cologne, Kerpener Str. 62, 50937 Cologne, Germany

⁵ Philips Clinical Science CT, Haifa, Israel

⁶ Philips Clinical Science CT, Hamburg, Germany

Keywords Tomography, X-ray computed · Neoplasm metastasis · Spine · Image processing, computer-assisted · Magnetic resonance imaging

Abbreviations

CI	Conventional images
CNR	Contrast-to-noise ratio
DECT	Dual-energy computed tomography
DSCT	Dual-source computed tomography
MRI	Magnetic resonance imaging
PACS	Picture archiving and communication system
ROC	Receiver operating characteristic
SBI	Spectral base image
SDCT	Spectral detector computed tomography
VNCA	Virtual non-calcium images

Introduction

Contrast-enhanced computed tomography is the imaging method of choice for initial and follow-up imaging in oncologic patients. Iodine-based contrast agents are used to enhance soft tissue contrast, while the assessment of bone lesions remains challenging [1, 2]. Therefore, patients with high suspicions for bone metastasis frequently undergo additional imaging, e.g. magnetic resonance imaging (MRI), scintigraphy, or positron emission tomography [2].

New techniques such as dual-energy CT (DECT) may improve the assessment of bone lesions in CT by allowing for a multivariable material mapping, e.g., enabling subtraction of bone structures by use of calcium suppression, quantitation of iodine, and dedicated depiction of bone marrow or gadolinium [3–9]. Early results suggested that virtual non-calcium (VNCA) images might improve bone lesion assessment: Several studies investigated VNCA from dual-source computed tomography (DSCT) for visualization of bone marrow edema in degenerative and/or traumatic altered bone [10–14]. In an oncologic context, the benefit of VNCA images for the detection of bone marrow infiltration in multiple myeloma has been investigated on a DSCT system, representing an enhanced detection of pronounced diffuse bone marrow edema [4]. However, to the author's knowledge, no study conducted structured investigations of multi-level VNCA for investigating contrast-enhanced bone lesions such as metastases.

The goal of our study was to investigate the feasibility of VNCA from SDCT for the assessment of metastatic bone lesions in intra-individual comparison to non-metastatic bone using MRI as standard of reference.

Materials and methods

Patient identification

The institutional review board approved this mono-centric study; informed consent was waived due to its retrospective character. Identification of patients was performed based on a structured search within the picture archiving and communication system (PACS).

Inclusion criteria comprised (a) age ≥ 18 years, (b) SDCT and MRI of the corresponding region to serve as reference, and (c) examination between April 1, 2017, and August 30, 2017. The inclusion process and details on exclusion criteria are reported in Fig. 1. All examinations were carried out according to clinical indications; no scan was performed for the purpose of this study.

In total, 21 patients with a mean age of 56.0 ± 11.3 years, of which 15 were female, were included in this study. Cancer types comprised breast ($n = 8$), melanoma ($n = 5$), lung ($n = 4$), and colon ($n = 4$). Time difference between SDCT and MRI was 12 (5–56) days.

MRI protocol

All images were acquired using a 3.0-T MRI scanner using a body coil (Ingenia, Philips Healthcare). The imaging protocol included a sagittal short tau inversion recovery (STIR; time to repetition/inversion/echo, 3411/200/70 ms; slice thickness, 3 mm; gap, 0.3 mm) sequence, and an unenhanced sagittal T1-weighted turbo spin echo sequence (T1w; time of repetition/echo, 556/12 ms; slice thickness, 3 mm; gap, 0.3 mm). After review of the unenhanced acquisitions, a body weight-adapted volume of gadolinium-based contrast agent (Dotarem, 0.2 mg/kg body weight, Guerbet) was administered through a peripheral vein and sagittal T1w as well as axial T1w mDixon imaging was performed on suspicious areas only (ceT1w, analogously to unenhanced T1w; axial T1 mDixon, time of repetition/echo, 687/10 ms; slice thickness, 3 mm; gap, 0.3 mm).

SDCT imaging protocol

CT imaging was performed using a spectral detector CT (IQon, Philips). Patients were scanned in a supine, head-first position. For contrast-enhanced studies, a body weight-adapted volume of non-ionic, iodine-based contrast media was applied through a cubital vein with a constant flow of 3.5 ml/s (Accupaque 350 mg/ml, GE Healthcare) followed by a 30-ml saline flush. Bolus tracking was applied using a

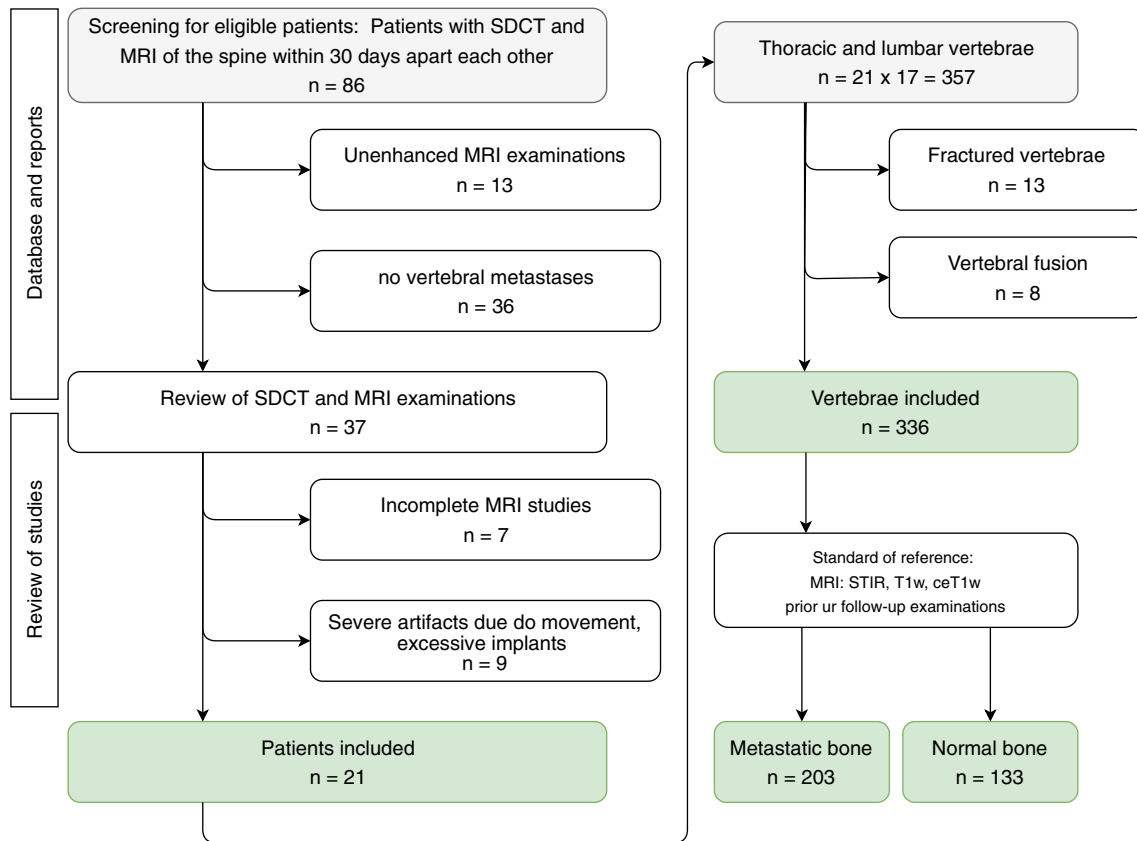


Fig. 1 Flowchart of inclusion and exclusion criteria for this study. After selection of patients (left), a more granular selection and classification were performed on a per vertebra basis (right)

region of interest within the descending aorta and a threshold value of 150 HU; scans were started with a delay of 50 s. Tube current modulation was applied in all examinations (DoseRight 3D-DOM; Philips Healthcare). Relevant scan parameters comprised collimation, 64×0.625 mm; rotation time, 0.5 s; pitch, 0.671; matrix, 512×512 ; tube voltage, 120 kVp; tube current, 116 mAs.

Establishment of a standard of reference

Conventional CT and MRI images (STIR, T1w, ceT1w) were viewed side by side in consensus by two radiologists with 5 and 8 years of experience in oncologic imaging. If bone exhibited unremarkable signal intensity in STIR, T1w, and ceT1w, it was considered normal. Lesions showing hyperintensity in STIR, hypointensity in unenhanced T1w, and enhancement after gadolinium administration were considered metastatic.

With the given 21 patients, there were a total of 357 vertebrae (5 lumbar, 12 thoracic) eligible for inclusions. Here, exclusion criteria comprised fractures or implants for vertebral fusions, resulting in a total of 336 vertebral bodies included in the final analysis, of which 203 were metastatic (Fig. 1).

SDCT image reconstruction and post processing

SDCT provides conventional image reconstructions by combining projection data from both detector layers and using a hybrid-iterative reconstruction algorithm with a constant kernel (referred to as CI; iDose⁴, level 3, Philips Healthcare). For dual-energy image post processing, a PACS-compatible file is generated, referred to as spectral base images (SBI). Technically, the SBI contains photoelectric-like and Compton-like images that allow for real-time post processing in the vendor's viewer (IntelliSpace Portal, Spectral Diagnostics Suite, Philips Healthcare). All SDCT images were reconstructed with a slice thickness and section increment of 2 mm.

We used a prototype image re-composition algorithm that allows for reconstruction of VNCA images based on these SBI files. It employs the acquired spectral data to identify and suppress calcium by replacing the HU of voxels containing calcium with a virtual HU value as similar as possible to the expected HU without calcium contribution to the attenuation. Further, it allows to freely choose a calcium suppression index. While a low calcium suppression index targets tissues with a low calcium composition weight, a high index value targets tissues with a high calcium composition weight.

The computation of VNCA images is described in detail elsewhere [4, 14]. A pre-defined soft tissue material and a user-defined target level of calcium content (indicated by the calcium suppression index) are converted to corresponding attenuation values using the National Institute of Standards and Technology database. These are then projected to the SDCT photoelectric- and scatter-like decomposition functions (CaVector). As in all DECT systems, each material is defined by a vector representing the ratio photoelectric- and scatter-like component while its magnitude represents the quantities of the materials. The VNCA image is then derived using the calculated attenuation at 70 keV for all voxels leaving out any attenuation corresponding to the CaVector.

For this study, images were reconstructed with a low (level 25), medium (level 50), and high (level 90) calcium suppression index (referred to as VNCA^{low}, VNCA^{med}, VNCA^{high}, respectively). All images were reconstructed in the sagittal plane (slice thickness, 3 mm).

Objective image assessment

Objective image analysis was carried out based on a circular region of interest (ROI) with a size of 100 mm² (size was possibly reduced to avoid unrepresentative tissue). A maximum of three ROI per patient was drawn in each normal and metastatic trabecular bone on CI (NORM and MET, respectively). The ROI were then copied and pasted to identical positions in VNCA. From each ROI, averaged attenuation (HU) and standard deviation (SD) were recorded. To evaluate the separation between normal and metastatic bone, a modified contrast-to-noise ratio (mCNR) was calculated to represent differences between normal and metastatic bone as $mCNR = \frac{|HU_{MET} - HU_{NORM}|}{\sqrt{(SD_{MET})^2 + (SD_{NORM})^2}}$, adapted from earlier studies [15, 16].

Subjective image assessment

After objective image analysis was completed, two readers with 3 and 8 years of experience in oncologic imaging independently reviewed CI, VNCA^{low}, and VNCA^{med} images in sagittal plane and were asked to determine the presence of a suspicious bone lesion on a per vertebra basis using a binary scale. VNCA^{high} images were excluded from final analysis due to their poor performance in objective analysis. Due to their characteristic appearance, readers were not blinded regarding the calcium suppression indices. Different reconstructions were interpreted in three different sessions with a minimum of 2 weeks apart from each other to avoid a recall bias. The readers were explicitly free to adjust window center and width for all image reconstructions.

Statistic assessment

Interval scaled data is reported as mean \pm standard deviation. Statistical analysis was performed using JMP (SAS Institute) and MedCalc (MedCalc Software). Student's *T* test or ANOVA with Tukey HSD adjustment for multiple comparisons was used to compare interval scaled data. For objective analysis, sensitivity and specificity were calculated and receiver operating characteristic (ROC) curves were analyzed; the area under the curve was compared using DeLong's method. For subjective analysis, pooled sensitivity and specificity from both readers were calculated. Youden's index was used to determine optimal cut-off values for the CT numbers in VNCA reconstructions [17]. Statistic comparison of subjective analysis was conducted using McNemar's test. A $p \leq 0.05$ was considered to be statistically significant. Cohen's kappa was calculated to determine inter-rater reliability and interpreted as earlier suggested: excellent ($\kappa \geq 0.8$), good ($\kappa \geq 0.6$), moderate ($\kappa \geq 0.4$), and poor ($\kappa < 0.4$) [18–20].

Results

Objective image analysis

On conventional images, attenuation within normal and metastatic bone ranged from -46.3 to 238.8 HU (109.8 ± 60.1 HU), exhibiting a large overlap while CT numbers for VNCA^{low} showed a wider range (-343.3 to 60.2 HU (-163.5 ± 103.2 HU); $p \leq 0.05$; Fig. 2). Ranges for VNCA^{med} and VNCA^{high} were rather small (-89.0 to 42.6 HU and -25.9 to 64.6 HU, respectively; further details in electronic supplement 1).

Noise for normal and metastatic bone was comparable with CI and VNCA^{low} (24.6 ± 11.4 HU and 29.6 ± 16.1 HU, $p = 0.451$), while VNCA^{med} and VNCA^{high} exhibited lower image noise as compared with CI (17.5 ± 6.1 HU and 17.5 ± 9.2 HU, $p \leq 0.05$; further details in electronic supplement 1).

Overlap between normal and metastatic bone was smaller in VNCA^{low} and VNCA^{med} as compared with CI and VNCA^{high}. The latter showed the largest overlap, indicating an impaired separation of normal and metastatic bone (Fig. 2; further details in electronic supplement 1). mCNR was able to further substantiate a significantly improved differentiability in VNCA^{low} (Fig. 3a; further details in electronic supplement 1).

Further, the discrimination of normal versus metastatic bone as illustrated by the area under the curve in ROC analysis was significantly higher in VNCA^{low} and VNCA^{med} as compared with CI and VNCA^{high} (Fig. 3b; CI vs VNCA^{low}, 0.74 vs 0.95 , $p \leq 0.05$; VNCA^{low} vs VNCA^{med}, 0.95 vs 0.98 , $p \geq 0.05$; VNCA^{med} vs VNCA^{high}, 0.98 vs 0.73 , $p \leq 0.05$; CI vs VNCA^{high}, 0.74 vs 0.73 , $p \geq 0.05$). Ideal cut-off values were identified by determination of Youden's index for all reconstructions. Youden's index was found to be highest in

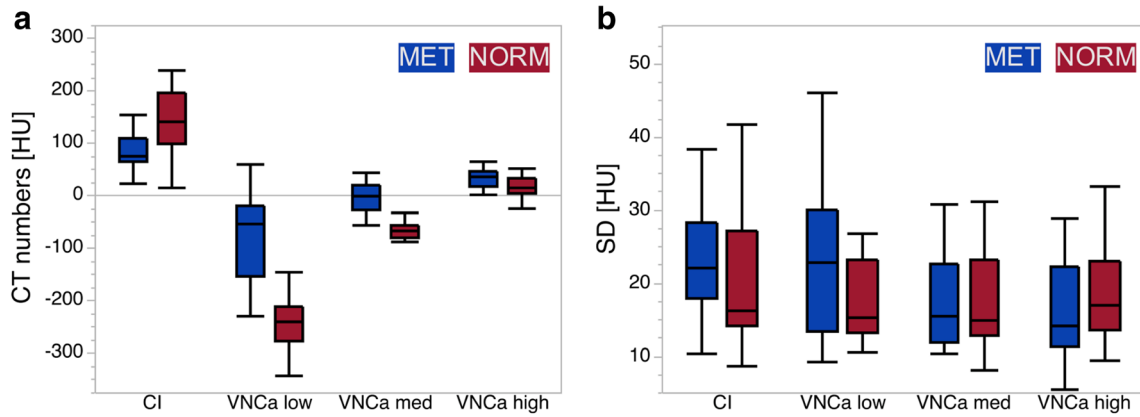


Fig. 2 a Imaging characteristics of normal and metastatic bone CT numbers for normal and metastatic bone (NORM and MET) in conventional images (CI) and virtual non-calcium (VNCA) images with

different calcium suppression indices (low, medium, and high). **b** Further, the standard deviation in the different measurements is reported

VNCA^{low} and VNCA^{med} (CI 89.6, 115.3; VNCA^{low} - 174.9, - 143.2; VNCA^{med} - 39.2, - 30.8; VNCA^{high} 24.8; [two values are reported if Youden’s index had two maxima]).

Discussion

Subjective image analysis

This study investigated multi-level calcium suppression in SDCT images and its benefit in assessing vertebral metastases. We found that calcium can be suppressed in SDCT images using the investigated prototype post processing algorithm. The obtained images allow for a better discrimination of normal and metastatic bone as indicated by ROC analysis. Further, subjective assessment demonstrated improved sensitivity and specificity as compared with CI, however, only if using low-level calcium suppression indices (level 25). This is of particular interest, since Neuhaus et al using the same scanner and a comparable imaging protocol reported that high-level calcium suppression (level 70–100) is recommended for the detection of fracture-associated edema [4].

In CI, readers correctly identified 78% of metastatic vertebrae with a specificity of 82%. VNCA^{low} yielded a clear improvement in sensitivity to 85% while specificity increased slightly as well (84%, $p \leq 0.05$ and $p > 0.05$, respectively) (Figs. 4 and 5). VNCA^{med} showed a decrease in sensitivity while specificity increased (71% and 88%, both $p \leq 0.05$, respectively). Detailed reports on outcome of subjective analysis are summarized in Table 1. Inter-rater reliability was good ($\kappa = 0.630$ –0.653; Table 1).

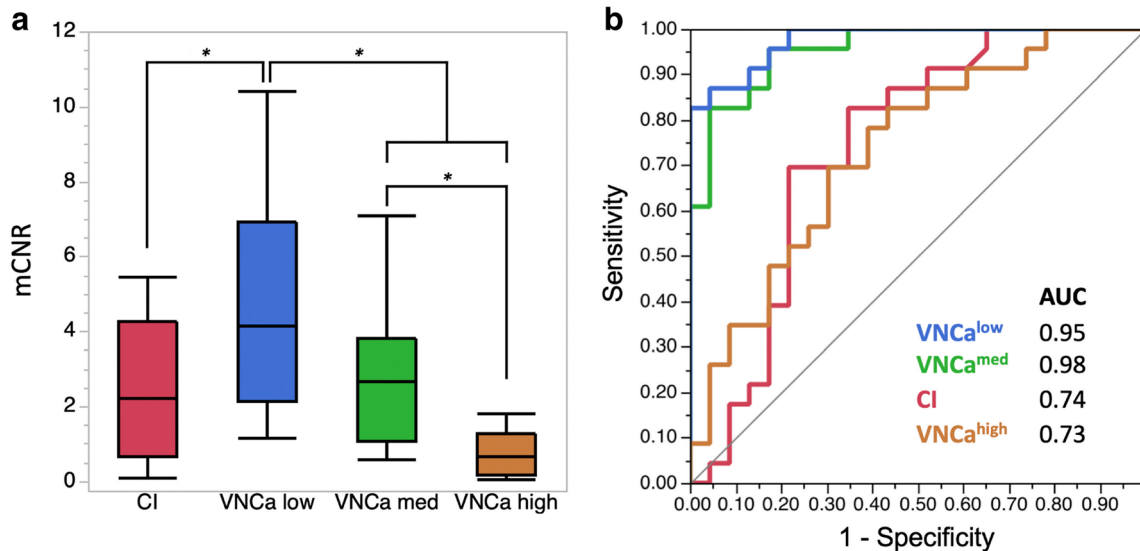


Fig. 3 a Contrast between normal and metastatic bone (as indicated by the modified contrast-to-noise ratio, mCNR) was improved in virtual non-calcium images with a low calcium suppression index (VNCA low) as compared with

conventional images (CI) and different calcium suppression indices. Significant differences as indicated by ANOVA are shown and indicated by an asterisk ($p \leq 0.05$). **b** Receiver operating characteristics substantiate this finding further by comparing the area under the curve (AUC)

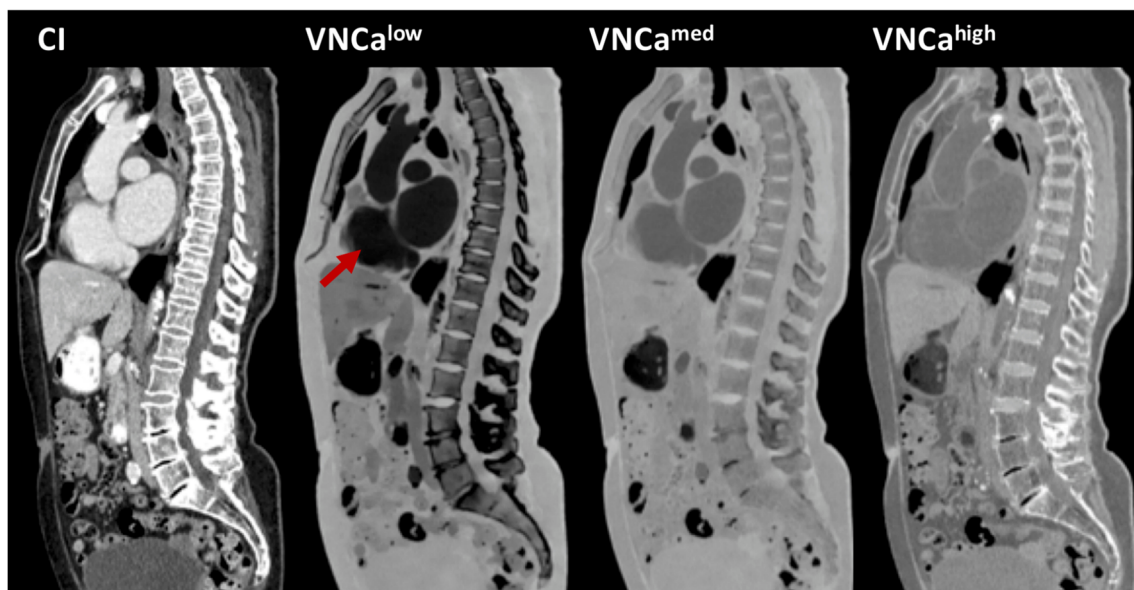


Fig. 4 Conventional and virtual non-calcium images. Sagittal image reconstructions of a 58-year-old patient as conventional images (CI) and virtual non-calcium images with different calcium suppression indices

(VNCA low, medium, and high). Notably, iodine is suppressed in low indices illustrating the limits of spectral separation (arrow in VNCA low)

The reason for this is likely the closeness of the attenuation profiles of calcium and iodine; therefore, higher calcium suppression levels may suppress iodine content along with calcium content. Material decomposition is limited by the spectral capability, which is inherent to the used DECT technique [3]. Tube-modifying setups allow for a modification and therefore improvement of spectral separation in a wide range (70–140 kV) [5, 21, 22]. In SDCT, the spectral separation is an inherent characteristic of the dual-layer detector [23, 24]. According to the vendor, the separation between low- and high-energy photons is optimized in a way that both detector layers exhibit comparable noise characteristics when examining an adult. Naturally, this results in an overlap of low- and high-energy photon spectra; however, besides spectral overlap, noise plays a crucial role in the spectral capability of any DECT system as noise arises from various factors which add quadratically [14, 25]. Due to the temporospatial coherence of low- and high-energy datasets inherent to the concept of the dual-layer detector, anti-correlation of noise can be exploited for image reconstruction resulting in a considerable decrease of image noise which in turn increases spectral capability [16, 26–30]. Outside bone, the capability and accuracy of SDCT for material decomposition have been demonstrated earlier in phantoms for iodine and gadolinium and for urinary concrements [8, 30, 31]. In contrast to the detection of bone metastases, the use of calcium suppression for the detection of diffuse bone edema needs targeted calcium suppression to the bone mineral content [4], and usually targets at the highest calcium suppression indices. Although different DECT systems vary with respect to spectral separation, noise, and temporal and/or spatial misalignment, a multi-level calcium

suppression in order to allow for a better delineation of metastases may be beneficial to these DECT approaches as well.

Subjective image analysis substantiated the objective findings showing an improvement of both sensitivity and specificity using VNCA^{low}. Nevertheless, it needs to be emphasized that conventional images need to be reviewed in the first place and independently since they represent the standard of care. In a meta-analysis, Yang et al reported sensitivity and specificity regarding the detection of metastasis on conventional CT images of 77.1% and 83.2% [32]. Their reports correspond well to obtained values in our analysis using CI; however, by using VNCA^{low}, we found values clearly higher which further substantiates our objective analysis and a benefit from calcium suppression in CT imaging [5, 32]. Besides VNCA, there are other tools and software such as temporal subtraction toolkits available which may further improve diagnostic performance [33, 34]. To use VNCA images in daily routine, overlay with conventional images may be especially helpful since they can help to raise suspicion in patients with known metastatic disease. While we demonstrated that VNCA^{low} images from SDCT improve visualization and detection of vertebral metastases, future large-scale studies are necessary to understand possible pitfalls of the algorithm and the impact of the technology on follow-up investigations in the clinical routine. Another limitation of this study is that only lesions within the vertebral body were included. In line with earlier studies, we used MRI as a reference standard, but could not obtain histologic proof of every lesion [5, 6, 10, 35]. Due to the small sample size, we were unable to perform a subgroup analysis to differentiate between malignant diseases. It remains elusive if VNCA images provide a particular benefit for a specific

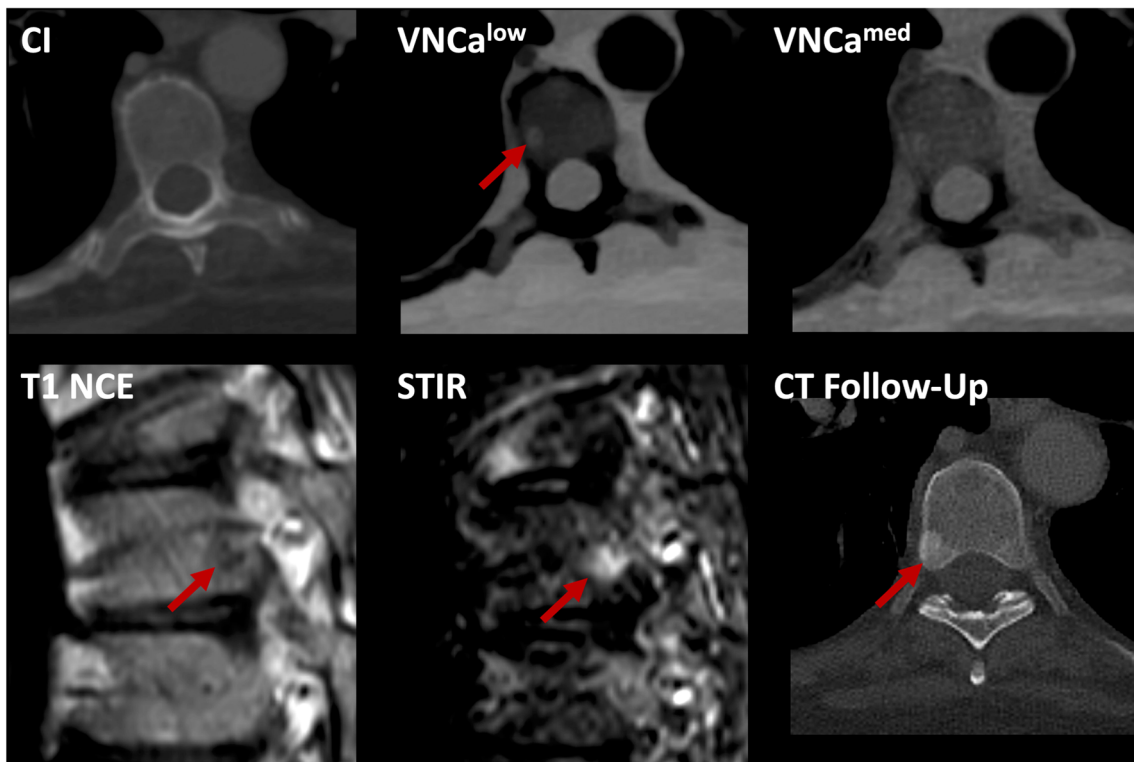


Fig. 5 Multimodality imaging of a metastasis in thoracic vertebra 6. Image of a 63-year-old female patient with a metastasis in thoracic vertebra 6. The lesion is not visible in the conventional image (CI), while the virtual non-calcium image with low calcium suppression index clearly illustrates the small metastasis in the right posterior portion of the vertebral body (VNCA^{low}); however, applying moderate or high calcium

suppression indices, the metastasis is not visible either (VNCA^{med}). Sagittal MRI corresponds well with non-contrast-enhanced T1 hypointensity and hyperintensity in STIR imaging (T1 NCE and STIR, respectively). Follow-up CT after radiation therapy clearly demonstrates osteoblastic changes (CT follow-up)

cancer, and larger, more specific studies are encouraged to investigate this.

This is one of the first studies to investigate calcium subtraction in SDCT examinations. We demonstrated feasibility

of calcium suppression in SDCT and that such images are capable to improve differentiation between metastatic and normal bone. Multi-level VNCA assessment reconstructed from SDCT improved separation of normal and metastatic

Table 1 Sensitivity, specificity, and inter-rater reliability (Cohen’s kappa) for conventional images (CI) and virtual non-calcium (VNCA) images with different strengths (low and medium). In addition, 95% confidence

intervals for sensitivity and specificity and the area under the curve are reported. An asterisk indicates significant differences as compared with CI

		Reader 1	Reader 2	Combined	Lower 95% confidence interval	Upper 95% confidence interval
CI	Sensitivity	0.76	0.80	0.78*	0.73	0.82
	Specificity	0.89	0.75	0.82*	0.77	0.87
	Cohen’s kappa			0.63*		
	Area under the curve (AUC)			0.80*	0.75	0.84
VNCA ^{low}	Sensitivity	0.86	0.83	0.85*	0.81	0.88
	Specificity	0.89	0.79	0.84*	0.79	0.88
	Cohen’s kappa			0.65*		
	Area under the curve (AUC)			0.84*	0.83	0.88
VNCA ^{med}	Sensitivity	0.69	0.73	0.71*	0.67	0.76
	Specificity	0.91	0.86	0.88*	0.84	0.92
	Cohen’s kappa			0.63*		
	Area under the curve (AUC)			0.75*	0.80	0.84

bone and diagnostic performance when using low to intermediate calcium suppression indices.

Funding Part of this study have been funded under a research agreement between (i) University Hospitals Cleveland Medical Center/Case Western Reserve University and Philips Healthcare and (ii) University Hospital Cologne and Philips Healthcare.

Compliance with ethical standards

Guarantor The scientific guarantor of this publication is PD Dr. med. Jan Borggrefe.

Conflict of interest The authors of this manuscript declare relationships with the following companies: NGH, DM, JB are on the speakers bureau of Philips Healthcare. ZR, GP are employees of Philips Healthcare.

Statistics and biometry One of the authors has significant statistical expertise.

Informed consent Written informed consent was waived by the Institutional Review Board.

Ethical approval Institutional Review Board approval was obtained.

Methodology

- retrospective
- experimental
- performed at one institution

References

- Hopper KD, Singapuri K, Finkel A (2000) Body CT and oncologic imaging. *Radiology* 215:27–40. <https://doi.org/10.1148/radiology.215.1.r00ap1727>
- Heindel W, Gübitz R, Vieth V, Weckesser M, Schober O, Schäfers M (2014) The diagnostic imaging of bone metastases. *Dtsch Arztebl Int* 111:741–747. <https://doi.org/10.3238/arztebl.2014.0741>
- Borggrefe J, Neuhaus V, Le Blanc M et al (2018) Accuracy of iodine density thresholds for the separation of vertebral bone metastases from healthy-appearing trabecular bone in spectral detector computed tomography. *Eur Radiol*. <https://doi.org/10.1007/s00330-018-5843-y>
- Neuhaus V, Lennartz S, Abdullayev N et al (2018) Bone marrow edema in traumatic vertebral compression fractures: diagnostic accuracy of dual-layer detector CT using calcium suppressed images. *Eur J Radiol* 105:216–220. <https://doi.org/10.1016/j.ejrad.2018.06.009>
- Kosmala A, Weng AM, Heidemeier A et al (2017) Multiple myeloma and dual-energy CT: diagnostic accuracy of virtual noncalcium technique for detection of bone marrow infiltration of the spine and pelvis. *Radiology* 0:170281. <https://doi.org/10.1148/radiol.2017170281>
- Petritsch B, Kosmala A, Weng AM et al (2017) Vertebral compression fractures: third-generation dual-energy CT for detection of bone marrow edema at visual and quantitative analyses. *Radiology* 284:161–168. <https://doi.org/10.1148/radiol.2017162165>
- Zhang LJ, Wang ZJ, Lu L, Chen B, Lu GM (2011) Feasibility of gadolinium-enhanced dual energy CT pulmonary angiography: a pilot study in rabbits. *Int J Cardiovasc Imaging* 27:1069–1080. <https://doi.org/10.1007/s10554-010-9755-4>
- van Hamersvelt RW, Willeminck MJ, de Jong PA et al (2017) Feasibility and accuracy of dual-layer spectral detector computed tomography for quantification of gadolinium: a phantom study. *Eur Radiol* 27:3677–3686. <https://doi.org/10.1007/s00330-017-4737-8>
- Mei K, Schwaiger BJ, Kopp FK et al (2017) Bone mineral density measurements in vertebral specimens and phantoms using dual-layer spectral computed tomography. *Sci Rep* 7:17519. <https://doi.org/10.1038/s41598-017-17855-4>
- Dareez NM, Dahlslett KH, Engesland E, Lindland ES (2017) Scaphoid fracture: bone marrow edema detected with dual-energy CT virtual non-calcium images and confirmed with MRI. *Skeletal Radiol*. <https://doi.org/10.1007/s00256-017-2730-6>
- Zbijewski W, Sisniega A, Stayman JW et al (2015) Dual-energy imaging of bone marrow edema on a dedicated multi-source cone-beam CT system for the extremities. *Proc SPIE Int Soc Opt Eng*. <https://doi.org/10.1117/12.2082304>
- Wang CK, Tsai JM, Chuang MT, Wang MT, Huang KY, Lin RM (2013) Bone marrow edema in vertebral compression fractures: detection with dual-energy CT. *Radiology* 269:525–533. <https://doi.org/10.1148/radiol.13122577>
- Reddy T, McLaughlin PD, Mallinson PI et al (2015) Detection of occult, undisplaced hip fractures with a dual-energy CT algorithm targeted to detection of bone marrow edema. *Emerg Radiol* 22:25–29. <https://doi.org/10.1007/s10140-014-1249-6>
- Hua CH, Shapira N, Merchant TE, Klahr P, Yagil Y (2018) Accuracy of electron density, effective atomic number, and iodine concentration determination with a dual-layer dual-energy computed tomography system. *Med Phys*. <https://doi.org/10.1002/mp.12903>
- Sudarski S, Apfalter P, Nance JW Jr et al (2014) Objective and subjective image quality of liver parenchyma and hepatic metastases with virtual monoenergetic dual-source dual-energy CT reconstructions. An analysis in patients with gastrointestinal stromal tumor. *Acad Radiol* 21:514–522. <https://doi.org/10.1016/j.acra.2014.01.001>
- Große Hokamp N, Höink AJ, Doerner J et al (2017) Assessment of arterially hyper-enhancing liver lesions using virtual monoenergetic images from spectral detector CT: phantom and patient experience. *Abdom Radiol (NY)* 43:2066–2074. <https://doi.org/10.1007/s00261-017-1411-1>
- Hanley AJ, McNeil JB (1982) The meaning and use of the area under a receiver operating characteristic (ROC) curve. *Radiology* 143:29–36. <https://doi.org/10.1148/radiology.143.1.7063747>
- Fleiss JL, Cohen J (1973) The equivalence of weighted kappa and the intraclass correlation coefficient as measures of reliability. *Educ Psychol Meas* 33:613–619. <https://doi.org/10.1177/001316447303300309>
- Cohen J (1960) A coefficient of agreement for nominal scales. *Educ Psychol Meas* 20:37–46. <https://doi.org/10.1177/001316446002000104>
- Kottner J, Audige L, Brorson S et al (2011) Guidelines for reporting reliability and agreement studies (GRRAS) were proposed. *Int J Nurs Stud* 48:661–671. <https://doi.org/10.1016/j.ijnurstu.2011.01.016>
- McCullough CH, Leng S, Yu L, Fletcher JG (2015) Dual- and multi-energy CT: principles, technical approaches, and clinical applications. *Radiology* 276:637–653. <https://doi.org/10.1148/radiol.2015142631>
- Flohr TG, McCullough CH, Bruder H et al (2006) First performance evaluation of a dual-source CT (DSCT) system. *Eur Radiol* 16:256–268. <https://doi.org/10.1007/s00330-005-2919-2>
- Shefer E, Altman A, Behling R et al (2013) State of the art of CT detectors and sources: a literature review. *Curr Radiol Rep* 1:76–91. <https://doi.org/10.1007/s40134-012-0006-4>
- Carmi R, Naveh G, Altman A, Carmi R, Naveh G, Altman A (2005) Material separation with dual-layer CT. *IEEE Nucl Sci*

- Symp Conf Rec 4:1876–1878. <https://doi.org/10.1109/NSSMIC.2005.1596697>
25. Sellerer T, Noël PB, Patino M et al (2018) Dual-energy CT: a phantom comparison of different platforms for abdominal imaging. *Eur Radiol*. <https://doi.org/10.1007/s00330-017-5238-5>
 26. Kelcz F, Joseph PM, Hilal SK (1979) Noise considerations in dual energy CT scanning. *Med Phys* 6:418–425. <https://doi.org/10.1118/1.594520>
 27. Kalisz K, Rassouli N, Dhanantwari A, Jordan D, Rajiah P (2018) Noise characteristics of virtual monoenergetic images from a novel detector-based spectral CT scanner. *Eur J Radiol* 98:118–125. <https://doi.org/10.1016/j.ejrad.2017.11.005>
 28. Neuhaus V, Große Hokamp N, Abdullayev N et al (2017) Metal artifact reduction by dual-layer computed tomography using virtual monoenergetic images. *Eur J Radiol* 93:143–148. <https://doi.org/10.1016/j.ejrad.2017.05.013>
 29. Große Hokamp N, Hellerbach A, Gierich A et al (2018) Reduction of artifacts caused by deep brain stimulating electrodes in cranial computed tomography imaging by means of virtual monoenergetic images, metal artifact reduction algorithms, and their combination. *Invest Radiol* 53:424–431. <https://doi.org/10.1097/RLI.0000000000000460>
 30. Große Hokamp N, Salem J, Hesse A et al (2018) Low-dose characterization of kidney stones using spectral detector computed tomography: an ex vivo study. *Invest Radiol* 53:457–462. <https://doi.org/10.1097/RLI.0000000000000468>
 31. Pelgrim GJ, van Hamersvelt RW, Willeminck MJ et al (2017) Accuracy of iodine quantification using dual energy CT in latest generation dual source and dual layer CT. *Eur Radiol* 27:3904–3912. <https://doi.org/10.1007/s00330-017-4752-9>
 32. Yang HL, Liu T, Wang XM, Xu Y, Deng SM (2011) Diagnosis of bone metastases: a meta-analysis comparing 18F FDG PET, CT, MRI and bone scintigraphy. *Eur Radiol* 21:2604–2617. <https://doi.org/10.1007/s00330-011-2221-4>
 33. Ueno M, Aoki T, Murakami S et al (2018) CT temporal subtraction method for detection of sclerotic bone metastasis in the thoracolumbar spine. *Eur J Radiol*. <https://doi.org/10.1016/j.ejrad.2018.07.017>
 34. Akasaka T, Yakami M, Nishio M et al (2019) Detection of suspected brain infarctions on CT can be significantly improved with temporal subtraction images. *Eur Radiol* 29:759–769. <https://doi.org/10.1007/s00330-018-5655-0>
 35. Kaup M, Wichmann JL, Scholtz JE et al (2016) Dual-energy CT–based display of bone marrow edema in osteoporotic vertebral compression fractures: impact on diagnostic accuracy of radiologists with varying levels of experience in correlation to MR imaging. *Radiology* 280:510–519. <https://doi.org/10.1148/radiol.2016150472>

Publisher's note Springer Nature remains neutral with regard to jurisdictional claims in published maps and institutional affiliations.